

# Fluoride mediated conversion of $\text{FeOOH}$ into $\text{NiFeOOH}$ for outstanding oxygen evolution reaction



Benjamin Mulwa Kathale<sup>a</sup>, Hengbo Xiao<sup>a</sup>, Shengxiong Yang<sup>b</sup>, Hongxia Yin<sup>a</sup>, Tianshui Yu<sup>a</sup>, Xiangji Zhou<sup>a</sup>, Lihua Qian<sup>a,\*</sup>, Junwu Xiao<sup>b</sup>, Pengxiang Lei<sup>c</sup>, Xiuhong Li<sup>d</sup>

<sup>a</sup> School of Physics, Huazhong University of Science and Technology, Wuhan 430074, PR China

<sup>b</sup> Key Laboratory of Material Chemistry for Energy Conversion and Storage, Ministry of Education, Hubei Key Laboratory of Material Chemistry and Service Failure, Department of Chemistry and Chemical Engineering, Huazhong University of Science and Technology, Wuhan 430074, PR China

<sup>c</sup> School of Chemistry and Chemical Engineering, Hubei University of Technology, Wuhan 430068, PR China

<sup>d</sup> School of Mechanical Engineering, Hubei University of Technology, Wuhan 430068, PR China

## ARTICLE INFO

### Article history:

Received 19 October 2021

Revised 29 November 2021

Accepted 1 January 2022

Available online 7 January 2022

### Keywords:

Catalysis

Fluorinated nickel-iron-(Oxy)hydroxides

*In-situ* Raman spectroscopy

Oxygen evolution reaction

## ABSTRACT

By the use of different concentrations of F, we modulate the structure of NiFe catalysts to have a hybrid structure composed of different phases involved in Oxygen Evolution Reaction (OER) process. For the first time, *in-situ* Raman spectroscopy was used to study the structural change of the NiFe catalyst, associated with the effects of the concentration of F during the OER process. At a moderate concentration of F, it was found that; (1) the catalysts have a well-conductive hybrid structure composed of NiFeOOH ( $474\text{ cm}^{-1}$  and  $544\text{ cm}^{-1}$ ), FeOOH ( $715\text{ cm}^{-1}$ ) and  $\text{NiF}_2$  ( $310\text{ cm}^{-1}$ ) phases, and (2) F promotes an optimum mass ratio between Ni and Fe, which helps in the collaborative operation between Ni and Fe. This led to generation of catalysts with an optimum structure portraying excellent OER performance. Specifically, the synthesized catalysts required explicit low overpotential of 259 mV to generate current density of  $100\text{ mAcm}^{-2}$ , Tafel slope of  $60.3\text{ mVdec}^{-1}$ , high charge transfer rate signified by low resistance of  $1.46\text{ }\Omega$ , and high number of active OER sites implied by large double layer capacitance of  $2.90\text{ mF}$ . This study shades light to the understanding of the involved vital phases of F-NiFe catalysts and how F mediates the active phases during the OER process, hence contributing to the knowledge required for the designing of better catalysts for future electrodes.

© 2022 Elsevier Ltd. All rights reserved.

## 1. Introduction

Coupled NiFe-(oxy)hydroxide catalysts exhibit better oxygen evolution reaction (OER) performance than independent Ni and Fe (oxy)hydroxides due to the interaction between Ni and Fe ions [1]. Based on simulations, it has been found that Fe and Ni sites promote the formation of O active species and O-O coupling, respectively, hence accomplishing the OER process [2]. Consistent with the simulation conclusions, some experiments have confirmed the involvement of both Fe and Ni during the OER process [3–5].

Despite the admirable functionality of NiFe catalysts, further modification has been considered to boost their OER performance [6]; such as the use of dopants [7], strain [8], amorphous compounds [9], exfoliation [10], and defect engineering [11], as some of the approaches used to modify their chemical structure. It has been found that the inclusion of F atoms introduce defects into the

NiFe-(oxy)hydroxides [12–14]. For instance, Xu et al. investigated the structural change of NiFe catalyst after several Cyclic Voltammetry (CV) cycles, but only NiFeOOH phase was observed. The intensity of the phase increased during the electrochemical process which gives an indication of structural change on the NiFe catalyst [15]. Similarly, the same phase was observed by Qiu et al., although the NiFe catalyst was used without F doping [16]. Moreover, studies by Xiao et al. [13] and Wu et al. [17] pointed out that the concentration of F would affect the performance of the NiFe catalysts, but the real-time study investigating the influence of F on the catalysts during the OER process was not covered.

In this study, NiFe catalysts were synthesized with different concentrations (n) of F incorporated into the catalyst to form  $\text{Ni}_y\text{Fe}_x\text{OOH} - n\text{F}$  ( $\text{X-nF}$ ). The different concentrations (0 mM, 10 mM, 20 mM and 30 mM) of F precursor introduced into the NiFe catalysts were labelled as X-0F, X-10F, X-20F and X-30F, respectively. The synthesized catalysts were investigated by X-ray Photoelectron Spectroscopy (XPS), Scanning Electron Microscopy (SEM) and Transmission Electron Microscopy (TEM). The structural characterization of the catalysts before the OER process revealed

\* Corresponding author.

E-mail addresses: [jbenjahj@gmail.com](mailto:jbenjahj@gmail.com) (B.M. Kathale), [lhqian@mail.hust.edu.cn](mailto:lhqian@mail.hust.edu.cn) (L. Qian), [chjwxiao@hust.edu.cn](mailto:chjwxiao@hust.edu.cn) (J. Xiao).

the existence of FeOOH, Ni(OH)<sub>2</sub> and NiF<sub>2</sub> phases, which influence the performance of the catalysts during the OER process. Using the *in-situ* Raman spectroscopy during the OER process; (1) we determined the full structural change of Ni(OH)<sub>2</sub> and the partial structural change of FeOOH, (2) the sustained existence of NiF<sub>2</sub> was found to be influenced by the concentration of F, for the first time and (3) the existence of F was found to influence the concentration of Ni and Fe.

## 2. Experimental procedures

### 2.1. Catalyst fabrication

Ni foam pieces of 2 cm by 2 cm and a thickness of 1.6 mm were compressed to a thickness of 0.28 mm using 1klbs pressure source. The compression was to enable the catalyst stick to the Ni foam substrate. The compressed Ni foam pieces of substrate were immersed in 1.0 M H<sub>2</sub>SO<sub>4</sub> aqueous solution for 1 h to remove the surface residual oxides. The Ni foams were washed with deionized water to remove the acid solution on the surface. 20 mM iron nitrate hexahydrate (Fe(NO<sub>3</sub>)<sub>2</sub>•6H<sub>2</sub>O) and 10 mM sodium fluoride (NaF) were dissolved in 20 mL deionized water, aiming at synthesizing the Ni<sub>y</sub>Fe<sub>x</sub>OOH-10F catalyst. Oxygen gas was bubbled through the solution for a period of 10 min. The compressed and washed Ni foam substrate pieces were immersed into the solution at room temperature and oxygen gas allowed to flow on the surface of the solution for 12 h. The samples were washed with deionized water. The resulting sample was labeled as Ni<sub>y</sub>Fe<sub>x</sub>OOH-10F. In a similar way, the Ni<sub>y</sub>Fe<sub>x</sub>OOH-0F, Ni<sub>y</sub>Fe<sub>x</sub>OOH-20F and Ni<sub>y</sub>Fe<sub>x</sub>OOH-30F samples were synthesized by changing the NaF concentration as 0 (NaF not added), 20 mM and 30 mM, respectively.

### 2.2. Sample characterization

The XPS was conducted using Thermo Scientific™ K-Alpha™ XPS system, with a resolution of 0.3–0.5 eV generated by monochromated Al anode X-ray source, whose K $\alpha$  radiation energy was 1486.6 eV. A Bruker X-ray diffraction (XRD) machine with Cu K $\alpha$  irradiation ( $\lambda=1.5406$  Å), operated at step size and scan rate of 0.05° and 0.025° s<sup>-1</sup>, respectively, was used to determine the XRD spectra of the samples. The SEM morphological imaging was carried out using Auriga 60 Crossbeam at an accelerating voltage of 3 kV. The TEM was carried out using Talos™ F200C at an accelerating voltage of 200 kV. The surface investigation was done using Raman spectroscope (Ramos S120, Ostec-ArtTool, LLC, Moscow) excited with 532 nm laser diode. The *in-situ* Raman spectroscopy during the OER process was conducted using the flow cell (C031-2, Gaoss Union, Tianjin).

### 2.3. Electrochemical and Raman spectroscopy tests

The electrochemical measurements were carried out on CHI 660E electrochemical workstation potentiostat (Chenhua Incorporation, China) in a three-electrode unit cell filled with approximately 25 ml of 1.0 M KOH electrolyte. The electrolyte was prepared by mixing KOH F.W.56.11 (Sinopharm Chemical Reagent Co. Ltd) with 18.5  $\Omega$  deionized water. The electrodes were; the working electrode, reference electrode (Hg/HgO) and counter electrode (graphite). Prior to the electrochemical tests, the catalysts were prepared by undertaking them through a CV process of 20 cycles at 20 mVs<sup>-1</sup> scan rate (Fig. S1), to remove the excess F. The Linear Sweep Voltammetry (LSV) and Cyclic Voltammetry (CV) measurements were done at 5 mVs<sup>-1</sup> scan rate and within 0–1 V (vs. Hg/HgO). The reference potential was determined using; E (vs. RHE) = E<sub>Hg/HgO</sub> + 0.0591  $\times$  pH + 0.098 V. Raman testing was done

using similar electrodes and electrolyte, as in the case of electrochemical analysis. Before and after investigating the OER process, Raman tests were done to help in comparing the structural change. During the OER process, the bias voltage was increased (while undertaking the corresponding Raman tests) from 0.4 V vs. Hg/HgO until no more meaningful spectrum was observed.

## 3. Results and discussion

Chemical bonding of the as-synthesized catalysts was investigated using XPS, and the corresponding peaks were tuned with C1s peak at 284.8 eV (Fig. S2). Fig. 1 shows the analysis for X-0F and X-20F while X-10F and X-30F are presented in Fig. S3 and Table S1. The occurrence of O1s peaks at 529.6 eV, 531.3 eV and 533 eV (for X-0F) and 529.4 eV, 531.4 eV and 532.6 eV (for X-20F) in Fig. 1(a) correspond to Fe/Ni-O, O-H and H<sub>2</sub>O bonding, respectively [13,17]. The Fe/Ni-O peak at 529.6 eV of the X-0F catalyst is found to shift to a lower binding energy (529.4 eV) and reduce in intensity after F-doping (X-20F). Similarly, the H<sub>2</sub>O peak (533.0 eV) for the X-0F catalyst is found to shift to a lower binding energy (532.6 eV), though its intensity increases. Since F doping leads to substituting the O elements with F [18], the doped F attracts more electrons as compared to O, making the bond to have more electrons and this may lead to the red-shift of the binding energy [19]. Moreover, the incorporation of O into the lattice may lead to the red-shift of the binding energy [14]. Interestingly, the O-H peak which influences the OER activity [20] is found to shift to a higher binding energy and since it supersedes the other peaks, the resultant effect of the O 1s peak is found to be a blue-shift. Fig. 1(b) shows the Ni-F bonding in F-doped catalyst (X-20F) at 684.4 eV which serves as an evidence of the formation of NiF<sub>2</sub> phase, but this was absent in the F-free catalyst [1,21].

Fig. 1(c) shows the existence of deconvoluted 2P<sub>3/2</sub> and 2P<sub>1/2</sub> orbitals together with their respective satellite (Sat.) peaks corresponding to Fe<sup>3+</sup>-O/OH bonding. The peaks 710.5 eV (2P<sub>3/2</sub>) and 724.1 eV (2P<sub>1/2</sub>) for the X-0F catalyst shift to peaks 712.6 eV (2P<sub>3/2</sub>) and 724.5 eV (2P<sub>1/2</sub>) in X-20F catalyst, correspond to the Fe<sup>3+</sup>-O bonding. In addition, peaks 712.5 eV (2P<sub>3/2</sub>) and 726.4 eV (2P<sub>1/2</sub>) for the X-0F catalyst shift to peaks 715.6 eV (2P<sub>3/2</sub>) and 727.5 eV (2P<sub>1/2</sub>) for the X-20F catalyst, correspond to Fe<sup>3+</sup>-OH bonding [14,22]. The existence of these peaks imply the formation of Fe<sub>2</sub>O<sub>3</sub> and FeOOH phases [23,24]. Fig. 1(d) shows the deconvoluted 2P<sub>3/2</sub> and 2P<sub>1/2</sub> peaks for the Ni 2P region. For X-0F catalyst, the peaks 855.7 eV (2P<sub>3/2</sub>) and 873.1 eV (2P<sub>1/2</sub>) which shift to 856.0 eV (2P<sub>3/2</sub>) and 873.4 eV (2P<sub>1/2</sub>) for the X-20F, respectively, correspond to the Ni<sup>2+</sup>-O bonding. Similarly, peaks 857.2 eV (2P<sub>3/2</sub>) and 874.4 eV (2P<sub>1/2</sub>) for the X-0F which shift to 857.9 eV (2P<sub>3/2</sub>) and 875.0 eV (2P<sub>1/2</sub>) for the X-20F, respectively, correspond to Ni<sup>2+</sup>-OH bonding [23,24], hence confirm the existence of the NiO and Ni(OH)<sub>2</sub> phases [22]. Comparing the 2P<sub>3/2</sub> and 2P<sub>1/2</sub> peaks of the F-free and F-doped catalysts, we find a shift to a higher binding energy due to the electronegativity effect of F [12]. F doping is found to attract electrons from the neighboring Fe and Ni cations [25], influencing their oxidation state, which leads to the blue shift of their binding energy [26]. In addition to the peak shift, the Full-Wave-Half-Maximum (FWHM) (Table S1) for each peak is found to change after the F-doping. Since the FWHM signifies the chemical or physical change of the surrounding environment of the chemical bond, therefore its of importance to note that the F-doping led to chemical change of the catalysts, which is also confirmed by the change of the chemical concentrations (%) as indicated at each peak in Table S1.

Moreover, the structural morphology of the catalysts was done using SEM, TEM and X-ray Diffraction (XRD). The SEM analysis shows different structures of the catalysts as presented in Fig. S4.

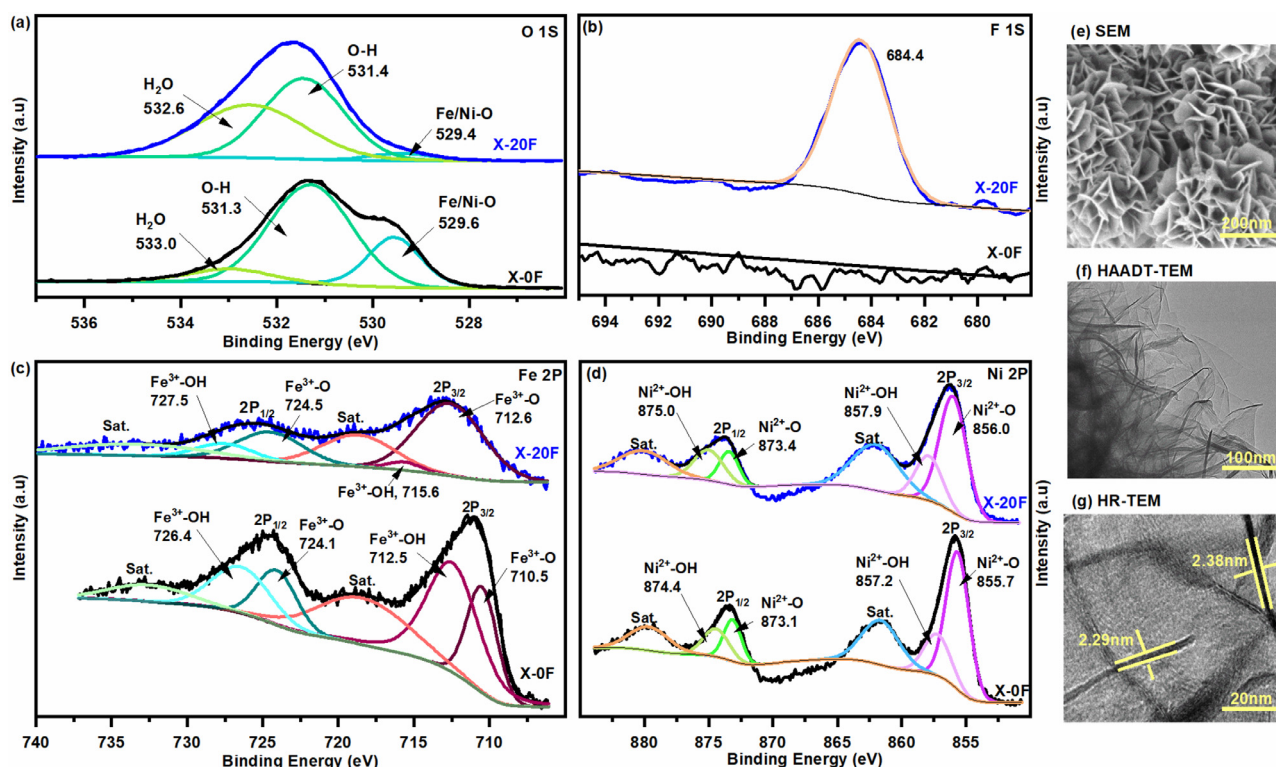


**Fig. 1.** Morphology and characterization before OER process: (a) O 1s, (b) F 1s, (c) Fe 2p and (d) Ni 2p XPS Regions for X-0F and X-20F Catalysts (Sat. represent satellite peaks). (e) SEM, (f) HAADF-STEM, and (g) HR-TEM images for the X-20F catalyst.

For the case of X-20F catalyst, Fig. 1(e) shows a spongy-like structure composed of vertically oriented nanosheets confirmed by the High-Angle Annular Dark-Field Scanning Transmission Electron Microscopy (HAADF-STEM) (Fig. 1(f)). The nanosheets are found to range between 2.29 nm and 2.38 nm thick as indicated by the High Resolution-TEM (HR-TEM) (Fig. 1(g)). The XRD analysis presented in Fig. S4, confirm the existence of different phases ( $\text{FeOOH}$ ,  $\text{Fe}_2\text{O}_3$ ,  $\text{Ni(OH)}_2$ ,  $\text{NiF}_2$ ) as indicated by the XPS analysis. The phases are found to be different in the respective catalysts, an influence attributed to the effect of F-doping. Consequently, the existence of the different phases in the catalysts necessitated the investigation of their OER performance.

The OER performance was evaluated by the use of LSV, CV, Electrochemical Impedance spectroscopy (EIS) and Electrochemical Surface Area (ECSA) approaches. At low voltages of LSV, Fig. 2(a) inset shows X-0F and X-10F catalysts having their anodic current increasing slightly while X-20F and X-30F having evident surge in the oxidation peaks. In all the catalysts, as the voltage increases the current density experiences a rapid surge at critical potential leading to oxygen evolution. Subjecting the catalysts to the same task to determine their OER performance, it was found that X-0F, X-10F, X-20F and X-30F required overpotential ( $\eta$ ) of 320 mV, 275 mV, 259 mV and 271 mV, respectively to generate 100  $\text{mA cm}^{-2}$  current density. Similarly, 105.6  $\text{mVdec}^{-1}$ , 72.4  $\text{mVdec}^{-1}$ , 60.3  $\text{mVdec}^{-1}$  and 68.7  $\text{mVdec}^{-1}$  Tafel slopes (b) correspond to X-0F, X-10F, X-20F and X-30F, respectively (Fig. 2(b)). Further, relating the F-free and F-doped catalysts, we found that the overpotential reduce by 14.1%, 19.1%, and 15.3% and Tafel slopes reduce by 31.4%, 42.9% and 34.9%, for X-10F, X-20F and X-30F, respectively (Table S2).

From the CV analysis, the catalysts are found to have different CV curves with oxidation ( $E_a$ ) and reduction ( $E_c$ ) peaks at different positions Fig. 2(c). The difference between the peaks ( $E_a - E_c$ ) for a given catalyst, relate to the structural deformation of the cat-

alyst [27]. The larger the difference, the more defective the catalyst is [27]. Fig. 2(c) inset, shows that X-20F has the largest peak difference (93 mV), hence the most defective. Beside, the shifting of the oxidation peaks presented in Fig. 2(c) to lower overpotential due to the concentration of F, signifies increase of Ni and decrease of Fe cations [5]. Moreover, the EIS results reveal X-20F has the lowest charge resistance of 1.46  $\Omega$  as compared to the other catalysts (Fig. 2(d)). Further, from the ECSA, we computed the double layer capacitance ( $C_{dl}$ ), a measure to determine the amount of OER active sites on the catalyst. The results show that X-20F has the largest capacitance of 2.90 mF (Fig. 2(e)), hence having the highest number of OER active sites. Therefore, based on the investigated OER performance parameters, we find that X-20F has the best OER performance parameters as summarized in Fig. 2(f). Furthermore, the X-20F catalyst was found to have the lowest overpotential ( $\eta$ ) of 259 mV to generate 100  $\text{mAcm}^{-2}$  and relatively low Tafel slope (b) of 60.3  $\text{mVdec}^{-1}$ . To concluded, we find that F-doping introduces defects that are subject to its concentration [15], hence boosting the OER performance [13]. A similar OER boosting effect was realized by doping the same NiFe catalysts with the other halogens (Cl, Br and I). Their performance followed the order of  $\text{F} > \text{Cl} > \text{Br} > \text{I}$  (Fig. S5). The OER performance of F-doped catalysts, necessitates an in-depth investigation on the chemical and structural change during the OER process using *in-situ* Raman spectroscopy.

Fig. 3(a–d) demonstrate the four catalysts with different peaks that correspond to different vibrations. The peaks at 500  $\text{cm}^{-1}$ , 510  $\text{cm}^{-1}$  and 530  $\text{cm}^{-1}$  are the Ni-O vibrational modes of the defective  $\text{Ni(OH)}_2$  phase [28,29]. 670  $\text{cm}^{-1}$ , 705  $\text{cm}^{-1}$ , 712  $\text{cm}^{-1}$  and 715  $\text{cm}^{-1}$  are vibrations associated with  $\text{Fe}_2\text{O}_3$  and  $\text{FeOOH}$  defective phase [21,30]. In addition, the fluorinated catalysts show a Raman peak at 310  $\text{cm}^{-1}$  associated with Ni-F vibrations of  $\text{NiF}_2$  phase [14,31]. At the onset of the OER bias potential, two new peaks appear: the stretching mode,  $A_{1g}$  (474  $\text{cm}^{-1}$ ) and the



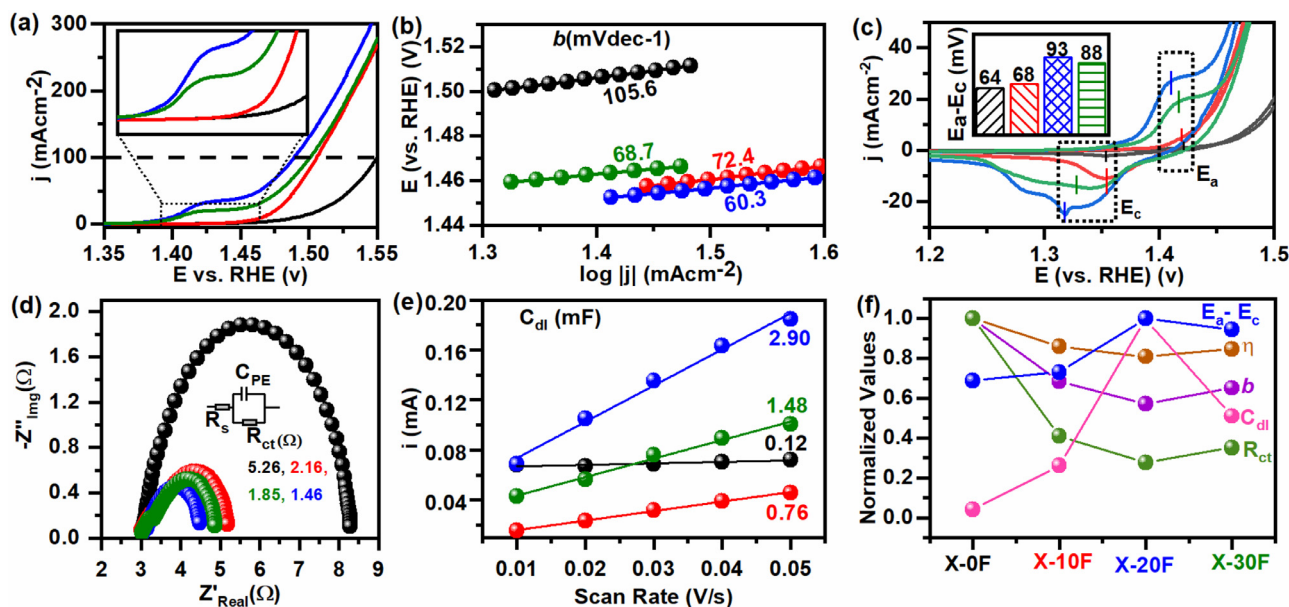


**Fig. 2.** Electrochemical applications and analysis: (a) LSV Spectra, (b) Tafel Slopes, (c) CV Spectra, (d) EIS, (e) Double layer capacitance, and (f) Normalized values for the OER performance measure parameters. (For (a–e), the spectrum in Black, Red, Blue and Green color represent X-0F, X-10F, X-20F and X-30F, respectively). (For interpretation of the references to color in this figure legend, the reader is referred to the web version of this article).

bending mode,  $E_g$  ( $544\text{ cm}^{-1}$ ), associated with  $\text{NiFeOOH}$  phase [28,29,32]. The observation of the Raman peaks made us to conclude that the catalysts have  $\text{Ni}(\text{OH})_2$ ,  $\text{Fe}_2\text{O}_3$ ,  $\text{FeOOH}$ ,  $\text{NiF}_2$  and  $\text{NiFeOOH}$  phases and are presented in Scheme S1.

Within the oxidation region (before OER onset potential), the catalysts were found to have  $\text{Ni}(\text{OH})_2$ ,  $\text{Fe}_2\text{O}_3$ ,  $\text{FeOOH}$  and  $\text{NiF}_2$  phases as confirmed by the Raman peaks. As the bias voltage increases to the OER region (after the OER onset potential),  $\text{Ni}^{2+}$  oxidizes to  $\text{Ni}^{3+}$  and Fe-oxide bonds break for F-free catalyst, leading to structural change from  $\text{Ni}(\text{OH})_2$  to  $\text{NiOOH}$  phase and from  $\text{Fe}_2\text{O}_3$  to  $\text{FeOOH}$  phase, respectively [33] (Fig. 3(a)). Some of the Fe cations generated from the broken Fe-oxide bonds, dope  $\text{NiOOH}$  to form  $\text{NiFeOOH}$  phase [15] evidenced by the change of positions of the  $474\text{ cm}^{-1}$  and  $544\text{ cm}^{-1}$  peaks (Fig. S6). For X-10F and X-30F catalysts, the chemical structures change from  $\text{Ni}(\text{OH})_2$ ,  $\text{NiF}_2$  and  $\text{FeOOH}$  to deformed  $\text{NiFeOOH}$  and  $\text{FeOOH}$  (Fig. 3(b & d)). A similar scenario as in the case of X-10 and X-30F, was seen with the X-20F catalyst, although the  $\text{NiF}_2$  phase was found to be evidently existing throughout all the bias voltages (Fig. 3(c)). The chemical and structural changes are confirmed by the disappearance and emergence of the related Raman peaks [33]. Moreover, the Ni-F bonds break leading to generation of Ni cations, which make the  $\text{NiOOH}$  phase amorphous [15]. Thus based on these observations, we concluded that the increase of the bias voltage leads to chemical and structural change [33].

The intensity ratio  $I_{474}/I_{544}$  (generated from Table S3), was used to show the degree of the structural disorder of the  $\text{NiFeOOH}$  phase [15]. The smaller the ratio, the more disordered the phase is. In this study, X-20F has the smallest ratio (0.27) compared to X-0F (0.77), X-10F (0.71) and X-30F (0.39) (Fig. 3(e)), hence the most disordered catalyst. This is consistent with the Reduction-Oxidation peak difference ( $E_a-E_c$ ) presented in Fig. 2(c). The good performance of X-20F catalyst, led to its chemical structure analysis using TEM. Fig. 3(f) is the High-Resolution Transmission Electron Microscopy (HR-TEM) image showing a nanostructure of the catalyst. The nanostructure is composed of different phases confirmed by different interplanar spacing ( $d$ ), whereby  $d = 0.231\text{ nm}$ ,  $0.257\text{ nm}$  and  $0.260\text{ nm}$  correspond to the crystal planes (102), (101) and (110) of  $\text{NiOOH}$  [34],  $\text{NiF}_2$  [35], and  $\text{FeOOH}$  [36] phases,

respectively. Furthermore, the structural image shows some sections with amorphous phases, which we assigned to the deformed  $\text{NiFeOOH}$  phase [36,37]. As argued out by others [38], we concluded that the structure was polycrystalline as confirmed by the presence of the concentric illustrations of its Fast Fourier Transform (FFT) (Fig. 3(f) inset). Moreover, we investigated the chronoamperometric stability for 24 h for the X-20F catalyst, which proved to be stable (Fig. 3(g)).

In addition, the area under the *in-situ* Raman peaks (Fig. S7) corresponding to  $\text{NiFeOOH}$ ,  $\text{FeOOH}$  and  $\text{NiF}_2$  phases presented in Fig. 3(a–d), was used to determine the relative intensity ratios of different chemical components in the catalysts. This helps in understanding the elemental compositional change between phases during the OER process. The compositional analysis is presented in Fig. 4.

As the bias voltage increases in each catalyst, the intensity of  $\text{FeOOH}$  decreases while  $\text{NiFeOOH}$  increases proportionally, verifying the transfer of Fe from  $\text{FeOOH}$  phase to  $\text{NiFeOOH}$  phase. This effect is confirmed by the relational change of  $\text{NiFeOOH}$  and  $\text{FeOOH}$  spectra (Fig. 4(a–d)). Comparing the F-free catalyst and the F-doped ones, we found that the concentration of Fe reduced in the fluorinated catalysts, depicted by the reduced ratio values of  $A_{\text{NiFeOOH}}/A_{\text{FeOOH}}$  (Fig. 4(e)), generated from Table S3). The higher the ratio, the more the Fe cations doped into the  $\text{NiFeOOH}$  phase. In this scenario, although X-0F has relatively smaller phase areas, the transfer of the Fe cations between the phases is the largest as compared to the F-doped catalysts. This implies that the concentration of F anions influence Fe cations, an effect attributed to their strong interaction coordination [13]. Considering the area ratios for the four catalysts (Fig. 4(e)), we find it consistent with the catalyst deformity relationship presented by Reduction-Oxidation peak difference ( $E_a-E_c$ ) (Fig. 2(c)) and  $I_{474}/I_{544}$  intensity ratios (Fig. 3(e)).

Moreover, from the F-doped catalysts (Fig. 4(b–d)), the intensity of  $\text{NiF}_2$  decreases as the voltage increases, confirming the breaking of Ni-F bonds, which lead to the increase of Ni cations on the catalyst [4], while F dissolves in the electrolyte as discussed by Xu et al. [15]. It's worth noting that, the intensity reduction of  $\text{NiF}_2$  in the X-10F and X-30F catalysts has a decay shape, contrary to that of the X-20F catalyst which reduces insignificantly and in a lineal

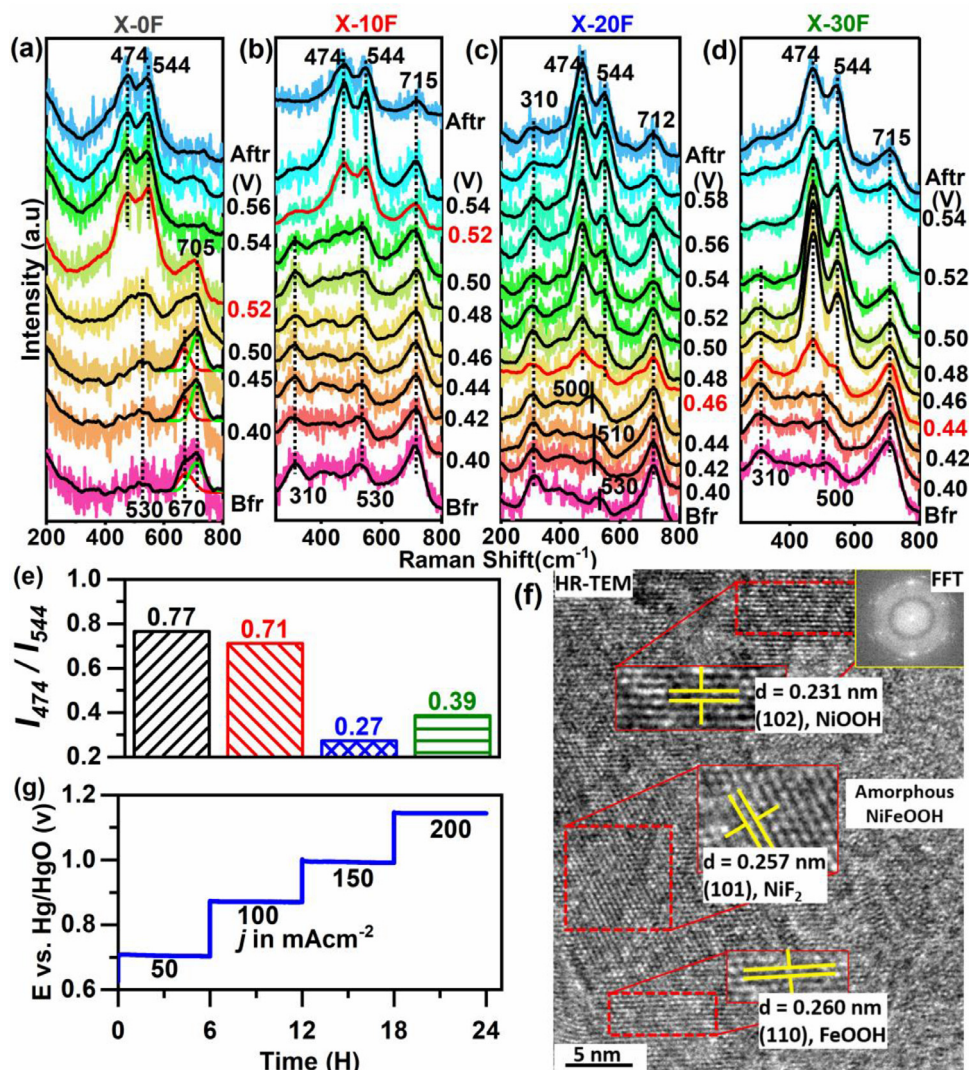


**Fig. 3.** (a–d) *In-situ* Raman Spectra obtained at different bias potentials (E vs. Hg/HgO) and (e) Peak Intensity ratios ( $I_{474}/I_{544}$ ) for all the catalysts. (f) HR-TEM and (g) Chronoamperometric stability test for 24 h, of the X-20F catalyst after the OER application.

manner. Therefore, the relative peak intensities confirm the relative ion transfer during the OER process, and can be used while analyzing the effect of F on the NiFe catalysts.

Founded on the chemical structures, the insights of how F influences the NiFe catalysts during the OER process is revealed by the *in-situ* Raman OER analysis in two ways; its influence on Fe and Ni cations, respectively. First, from the elemental analysis (Figs. 3 & 4), we find chemical and structural changes as the bias voltage increases. The Fe-oxide/hydroxide bonds are found to break and the generated Fe cations dope the NiFeOOH phase. With F-free catalysts, literature shows that too much of Fe cations leads to the formation of less active and poor conductive FeOOH phase, which negatively affects their OER performance [4]. Nevertheless, with the introduction of F, the quantity of Fe cations relatively reduce due to their strong interaction with the F anions [13], which in turn introduce defects on the FeOOH phase, making it more conductive [4], hence boosting the OER process. This makes the F-doped catalysts to have better OER performance as compared to F-free catalyst. In our findings, this effect is confirmed by the electrochemical results (Fig. 2(f)) presenting F-doped catalyst, X-30F (with relatively higher concentration of Fe than X-10F and X-20F, Fig. 4(e)) to have better OER performance than F-free catalyst, X-0F (with relatively highest concentration of Fe, Fig. 4(e)).

Second, the breaking of the Ni-F bonds increases the concentration of the Ni cations [4], making the NiOOH phase amorphous [15], and promoting the formation of O-OH and de-protonation of -OOH through electron withdrawal [4]. It creates defects which enhance ion diffusion and mass transport, hence boosting the OER process [12]. From Fig. 3(b & d), the Raman peak 310 cm<sup>-1</sup> corresponding to the Ni-F bonds in X-10F and X-30F, significantly reduces at the onset of OER, confirming the end of the generation of the Ni cations, as opposed to the X-20F catalyst which shows its existence in all the bias voltages. Consequently, for the X-20F catalyst, there is a continuous generation of the Ni cations in all the bias voltages (Fig. 3(c)). The existence of the NiF<sub>2</sub> phase at all bias voltages, promotes the OER activity, an effect attributed to; (1) the improvement of the intrinsic conductivity and (2) the regulatory of the adsorption energy of the active species in the catalyst [12], due to the easy breaking of Ni-F bonds which increases the OER active species [39].

Comparing the two effects of F on Ni and Fe, we find that F increases the Ni and reduces the Fe cations. At low F concentration, Ni cations are relatively less while Fe cations relatively more. As the concentration of F increases, Ni increase while Fe decrease as supported by the molar ratio Fe:Ni which is found to decrease as the concentration of F increases [13]. The effect of Ni and Fe



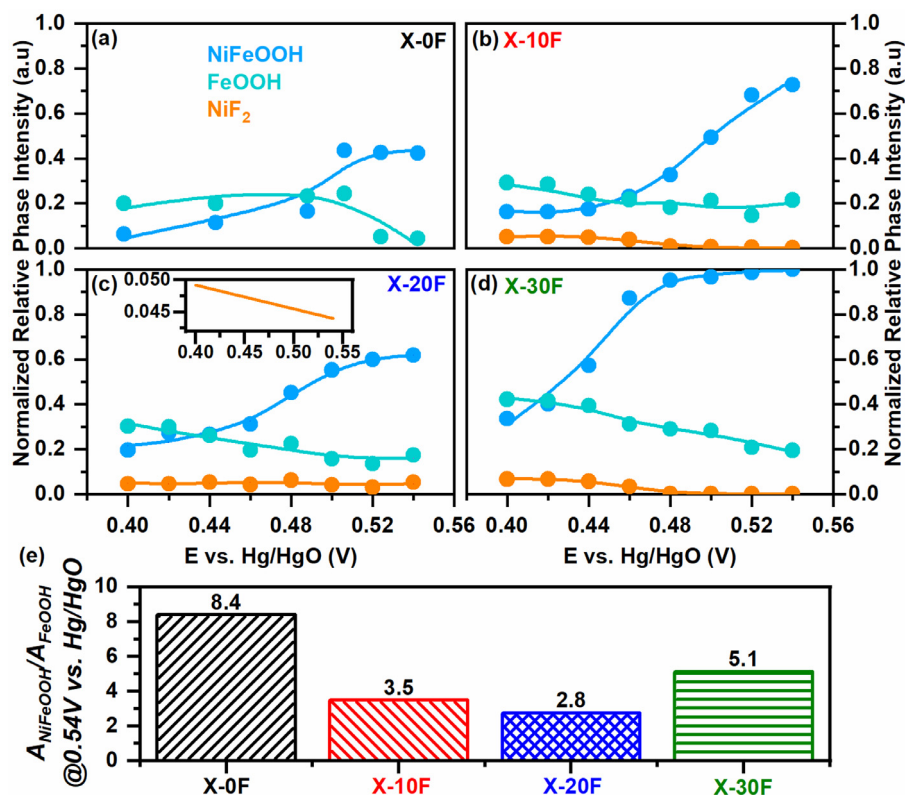


**Fig. 4.** Elemental Analysis of (a) NiFeOOH and NiOOH phases for X-0F, (b–d) NiFeOOH, NiOOH and NiF<sub>2</sub> phases for X-10F, X-20F and X-30F, and (e) Relative Area Ratio ( $A_{\text{NiFeOOH}}/A_{\text{FeOOH}}$ ) at a bias potential of 0.54 V vs. Hg/HgO. Inset (c) shows the magnified spectrum of NiF<sub>2</sub> phase.

concentrations in the NiFe catalysts, has been found to give an exponential growth-decay behavior [29]. In our OER analysis, this effect is evident by comparing the OER performance of the catalysts presented in Fig. 2(f). At low (X-10F) and high (X-30F) concentrations of F, the OER performance is low as compared to the moderate F concentration (X-20F). At higher F concentration, X-30F has low OER performance which resulted from the low Fe concentrations due to the strong coordination between the F anions and Fe cations with a stability constant of  $5.88 \times 10^{15}$  at 25 °C [13]. Based on this relationship, we concluded that the concentration of F facilitates the synergistic operation between Ni and Fe, where it was found that within moderate concentrations, the NiFe catalysts give the best OER performance as opposed to the low and high concentrations [40].

#### 4. Conclusion

In summary, the use of *in-situ* Raman spectroscopy determines the phase change in F-doped NiFe catalysts during OER. The F in NiF<sub>2</sub> (310 cm<sup>-1</sup>) were found to mediate the phase transition from FeOOH (715 cm<sup>-1</sup>) to NiFeOOH (474 cm<sup>-1</sup> and 544 cm<sup>-1</sup>). At moderate F concentration, the relative magnitudes of NiFeOOH and FeOOH phases were found to have an optimal balance, triggered by the F-controlled balanced concentration of Ni and Fe. This has a positive effect to the OER performance of the catalysts due to the synergistic operation between Ni and Fe. In general, the moderate concentration of F was found to improve the OER process of the catalysts by significantly lowering the overpotential (to 259 mV) required to generate current density of 100 mAcm<sup>-2</sup> and Tafel slope of 60.3 mVdec<sup>-1</sup>. Moreover, the catalysts had a high charge transfer rate and high number of active OER sites, implied by the low resistance of 1.46 Ω and large double layer capacitance of 2.90 mF, respectively. Therefore, the study demonstrated the ef-

fects of the concentrations of F in Ni-Fe catalysts, a key factor to be considered while synthesizing better performing electrodes.

#### Declaration of Competing Interest

There are no conflicts to declare.

#### Credit authorship contribution statement

**Benjamin Mulwa Kathale:** Conceptualization, Investigation, Methodology, Data curation, Formal analysis, Validation, Writing – original draft, Writing – review & editing. **Lihua Qian:** Supervision, Funding acquisition. **Junwu Xiao:** Supervision, Resources. **Pengxiang Lei:** Supervision, Resources.

#### Acknowledgment

Our appreciation goes to [National Natural Science Foundation of China](#) (21771069, 51771078 and 91545131) for the financial support and Shiyanjia Lab ([www.shiyanjia.com](http://www.shiyanjia.com)) for TGA, TEM, SEM and XPS characterization testing support. The first author acknowledges the financial support from [China Scholarship Council](#).

#### Supplementary materials

Supplementary material associated with this article can be found, in the online version, at [doi:10.1016/j.electacta.2022.139831](https://doi.org/10.1016/j.electacta.2022.139831).

#### References

- [1] H. Liu, M. Zha, Z. Liu, J. Tian, G. Hu, L. Feng, Synergistically boosting the oxygen evolution reaction of an Fe-MOF: via Ni doping and fluorination, *Chem. Commun.* 56 (2020) 7889–7892, [doi:10.1039/d0cc03422c](https://doi.org/10.1039/d0cc03422c).

- [2] H. Xiao, H. Shin, W.A. Goddard, Synergy between Fe and Ni in the optimal performance of (Ni,Fe)OOH catalysts for the oxygen evolution reaction, *Proc. Natl. Acad. Sci. U. S. A.* 115 (2018) 5872–5877, doi:[10.1073/pnas.1722034115](https://doi.org/10.1073/pnas.1722034115).
- [3] C. Kuai, Y. Zhang, D. Wu, D. Sokaras, L. Mu, S. Spence, D. Nordlund, F. Lin, X.W. Du, Fully oxidized Ni-Fe layered double hydroxide with 100% exposed active sites for catalyzing oxygen evolution reaction, *ACS Catal.* 9 (2019) 6027–6032, doi:[10.1021/acscatal.9b01935](https://doi.org/10.1021/acscatal.9b01935).
- [4] K. Zhang, R. Zou, Advanced transition metal-based OER electrocatalysts: current status, opportunities, and challenges, *Small* 2100129 (2021) 1–40, doi:[10.1002/sml.202100129](https://doi.org/10.1002/sml.202100129).
- [5] P. Acharya, Z.J. Nelson, M. Benamara, R.H. Manso, S.I.P. Bakovic, M. Abolhasani, S. Lee, B. Reinhart, J. Chen, L.F. Greenlee, Chemical structure of Fe-Ni nanoparticles for efficient oxygen evolution reaction electrocatalysis, *ACS Omega* 4 (2019) 17209–17222, doi:[10.1021/acsomega.9b01692](https://doi.org/10.1021/acsomega.9b01692).
- [6] F. Dionigi, P. Strasser, NiFe-based (Oxy)hydroxide catalysts for oxygen evolution reaction in non-acidic electrolytes, *Adv. Energy Mater.* 6 (2016), doi:[10.1002/aenm.201600621](https://doi.org/10.1002/aenm.201600621).
- [7] K. Fan, H. Chen, Y. Ji, H. Huang, P.M. Claesson, Q. Daniel, B. Philippe, H. Rensmo, F. Li, Y. Luo, L. Sun, Nickel-vanadium monolayer double hydroxide for efficient electrochemical water oxidation, *Nat. Commun.* 7 (2016) 1–9, doi:[10.1038/ncomms11981](https://doi.org/10.1038/ncomms11981).
- [8] D. Zhou, S. Wang, Y. Jia, X. Xiong, H. Yang, S. Liu, J. Tang, J. Zhang, D. Liu, L. Zheng, Y. Kuang, X. Sun, B. Liu, NiFe hydroxide lattice tensile strain: enhancement of adsorption of oxygenated intermediates for efficient water oxidation catalysis, *Angew. Chem. Int. Ed.* 58 (2019) 736–740, doi:[10.1002/anie.201809689](https://doi.org/10.1002/anie.201809689).
- [9] A. Indra, P.W. Menezes, N.R. Sahraie, A. Bergmann, C. Das, M. Tallarida, D. Schmeißer, P. Strasser, M. Driess, Unification of catalytic water oxidation and oxygen reduction reactions: amorphous beat crystalline cobalt iron oxides, *J. Am. Chem. Soc.* 136 (2014) 17530–17536, doi:[10.1021/ja509348t](https://doi.org/10.1021/ja509348t).
- [10] L. Hui, Y. Xue, B. Huang, H. Yu, C. Zhang, D. Zhang, D. Jia, Y. Zhao, Y. Li, H. Liu, Y. Li, Overall water splitting by graphdiyne-exfoliated and -sandwiched layered double-hydroxide nanosheet arrays, *Nat. Commun.* 9 (2018) 1–11, doi:[10.1038/s41467-018-07790-x](https://doi.org/10.1038/s41467-018-07790-x).
- [11] G. Ou, F. Wu, K. Huang, N. Hussain, D. Zu, H. Wei, B. Ge, H. Yao, L. Liu, H. Li, Y. Shi, H. Wu, Boosting the electrocatalytic water oxidation performance of CoFe<sub>2</sub>O<sub>4</sub> nanoparticles by surface defect engineering, *ACS Appl. Mater. Interfaces* 11 (2019) 3978–3983, doi:[10.1021/acsami.8b19265](https://doi.org/10.1021/acsami.8b19265).
- [12] C. Pei, Y. Gu, Z. Liu, X. Yu, L. Feng, Fluorinated iron–nickel layered double hydroxide for enhanced performance in the oxygen evolution reaction, *ChemSusChem* 12 (2019) 3849–3855, doi:[10.1002/cssc.201901153](https://doi.org/10.1002/cssc.201901153).
- [13] J. Xiao, A.M. Oliveira, L. Wang, Y. Zhao, T. Wang, J. Wang, B.P. Setzler, Y. Yan, Water-fed hydroxide exchange membrane electrolyzer enabled by a fluoride-incorporated nickel-iron oxyhydroxide oxygen evolution electrode, *ACS Catal.* 11 (2021) 264–270, doi:[10.1021/acscatal.0c04200](https://doi.org/10.1021/acscatal.0c04200).
- [14] K. Lemoine, J. Lhoste, A. Hémon-Ribaud, N. Heidary, V. Maisonneuve, A. Guiet, N. Kornienko, Investigation of mixed-metal (oxy)fluorides as a new class of water oxidation electrocatalysts, *Chem. Sci.* 10 (2019) 9209–9218, doi:[10.1039/c9sc04027g](https://doi.org/10.1039/c9sc04027g).
- [15] Q. Xu, H. Jiang, X. Duan, Z. Jiang, Y. Hu, S.W. Boettcher, W. Zhang, S. Guo, C. Li, Fluorination-enabled reconstruction of NiFe electrocatalysts for efficient water oxidation, *Nano Lett.* 21 (2021) 492–499, doi:[10.1021/acs.nanolett.0c03950](https://doi.org/10.1021/acs.nanolett.0c03950).
- [16] Z. Qiu, Y. Ma, T. Edvinsson, In operando Raman investigation of Fe doping influence on catalytic NiO intermediates for enhanced overall water splitting, *Nano Energy* 66 (2019) 104118, doi:[10.1016/j.nanoen.2019.104118](https://doi.org/10.1016/j.nanoen.2019.104118).
- [17] C. Wu, H. Li, Z. Xia, X. Zhang, R. Deng, S. Wang, G. Sun, NiFe layered double hydroxides with unsaturated metal sites via precovered surface strategy for oxygen evolution reaction, (2020), [10.1021/acscatal.0c02501](https://doi.org/10.1021/acscatal.0c02501).
- [18] X. Wang, X. Wang, Q. Di, H. Zhao, B. Liang, J. Yang, Mutual effects of fluorine dopant and oxygen vacancies on structural and luminescence characteristics of F doped SnO<sub>2</sub> nanoparticles, *Materials (Basel)* 10 (2017), doi:[10.3390/ma10121398](https://doi.org/10.3390/ma10121398).
- [19] B.H. McQuaide, M.S. Banna, The core binding energies of some gaseous aromatic carboxylic acids and their relationship to proton affinities and gas phase acidities, *Can. J. Chem.* 66 (1988) 1919–1922, doi:[10.1139/v88-309](https://doi.org/10.1139/v88-309).
- [20] D. Drevon, M. Görlin, P. Chernev, L. Xi, H. Dau, K.M. Lange, Uncovering the role of oxygen in Ni-Fe(OxHy) electrocatalysts using *in situ* soft X-ray absorption spectroscopy during the oxygen evolution reaction, *Sci. Rep.* 9 (2019) 1–11, doi:[10.1038/s41598-018-37307-x](https://doi.org/10.1038/s41598-018-37307-x).
- [21] B. Wei, C. Shang, X. Wang, G. Zhou, Conductive FeOOH as multifunctional inter-layer for superior lithium–sulfur batteries, *Small* 16 (2020) 1–10, doi:[10.1002/sml.202002789](https://doi.org/10.1002/sml.202002789).
- [22] P. Ganesan, A. Sivanantham, S. Shanmugam, Inexpensive electrochemical synthesis of nickel iron sulphides on nickel foam : super active and ultra-durable electrocatalysts for alkaline, (2016) 16394–16402, [10.1039/c6ta04499a](https://doi.org/10.1039/c6ta04499a).
- [23] K. Zhao, X. Ma, S. Lin, Z. Xu, L. Li, Ambient growth of hierarchical FeOOH/MXene as enhanced electrocatalyst for oxygen evolution reaction, *ChemistrySelect* 5 (2020) 1890–1895, doi:[10.1002/slct.201904506](https://doi.org/10.1002/slct.201904506).
- [24] W. Wang, Y. Wang, R. Yang, Q. Wen, Y. Liu, Z. Jiang, H. Li, T. Zhai, Vacancy-rich Ni(OH)<sub>2</sub> drives the electrooxidation of amino C–N bonds to nitrile C≡N bonds, *Angew. Chem. Int. Ed.* 59 (2020) 16974–16981, doi:[10.1002/anie.202005574](https://doi.org/10.1002/anie.202005574).
- [25] M. Li, H. Liu, L. Feng, Fluorination-induced high-performance catalysts for the oxygen evolution reaction: a mini review, *Electrochem. Commun.* 122 (2021) 106901, doi:[10.1016/j.elecom.2020.106901](https://doi.org/10.1016/j.elecom.2020.106901).
- [26] A.P. Grosvenor, M.C. Biesinger, R.S.C. Smart, N.S. McIntyre, New interpretations of XPS spectra of nickel metal and oxides, *Surf. Sci.* 600 (2006) 1771–1779, doi:[10.1016/j.susc.2006.01.041](https://doi.org/10.1016/j.susc.2006.01.041).
- [27] M.B. Stevens, C.D.M. Trang, L.J. Enman, J. Deng, S.W. Boettcher, Reactive Fe-sites in Ni/Fe (Oxy)hydroxide are responsible for exceptional oxygen electrocatalysis activity, *J. Am. Chem. Soc.* 139 (2017) 11361–11364, doi:[10.1021/jacs.7b07117](https://doi.org/10.1021/jacs.7b07117).
- [28] B.J. Trzecieński, O. Diaz-Morales, D.A. Vermaas, A. Longo, W. Bras, M.T.M. Koper, W.A. Smith, *In situ* observation of active oxygen species in Fe-containing Ni-based oxygen evolution catalysts: the effect of pH on electrochemical activity, *J. Am. Chem. Soc.* 137 (2015) 15112–15121, doi:[10.1021/jacs.5b06814](https://doi.org/10.1021/jacs.5b06814).
- [29] M.W. Louie, A.T. Bell, An investigation of thin-film Ni-Fe oxide catalysts for the electrochemical evolution of oxygen, *J. Am. Chem. Soc.* 135 (2013) 12329–12337, doi:[10.1021/ja405351s](https://doi.org/10.1021/ja405351s).
- [30] D. Thierry, D. Persson, C. Leygraf, N. Boucherit, A. Hugot-le Goff, Raman spectroscopy and XPS investigations of anodic corrosion films formed on FeMo alloys in alkaline solutions, *Corros. Sci.* 32 (1991) 273–284, doi:[10.1016/0010-938X\(91\)90073-X](https://doi.org/10.1016/0010-938X(91)90073-X).
- [31] M.J. Reisfeld, The absorption spectrum of potassium hexafluoronickelate(IV), *J. Mol. Spectrosc.* 29 (1969) 120–127, doi:[10.1016/0022-2852\(69\)90088-5](https://doi.org/10.1016/0022-2852(69)90088-5).
- [32] Y. Hao, Y. Li, J. Wu, L. Meng, J. Wang, C. Jia, T. Liu, X. Yang, Z.P. Liu, M. Gong, Recognition of surface oxygen intermediates on NiFe oxyhydroxide oxygen-evolving catalysts by homogeneous oxidation reactivity, *J. Am. Chem. Soc.* 143 (2021) 1493–1502, doi:[10.1021/jacs.0c11307](https://doi.org/10.1021/jacs.0c11307).
- [33] D. Friebe, M.W. Louie, M. Bajdich, K.E. Sanwald, Y. Cai, A.M. Wise, M.J. Cheng, D. Sokaras, T.C. Weng, R. Alonso-Mori, R.C. Davis, J.R. Bargar, J.K. Nørskov, A. Nilsson, A.T. Bell, Identification of highly active Fe sites in (Ni,Fe)OOH for electrocatalytic water splitting, *J. Am. Chem. Soc.* 137 (2015) 1305–1313, doi:[10.1021/ja511559d](https://doi.org/10.1021/ja511559d).
- [34] P.W. Menezes, S. Yao, R. Beltrán-Suito, J.N. Hausmann, P.V. Menezes, M. Driess, Facile access to an active γ-NiOOH electrocatalyst for durable water oxidation derived from an intermetallic nickel germanide precursor, *Angew. Chem.* 133 (2021) 4690–4697, doi:[10.1002/ange.202014331](https://doi.org/10.1002/ange.202014331).
- [35] H. Liu, Z. Liu, L. Feng, Bonding state synergy of the NiF<sub>2</sub>/Ni<sub>2</sub>P hybrid with the co-existence of covalent and ionic bonds and the application of this hybrid as a robust catalyst for the energy-relevant electrooxidation of water and urea, *Nanoscale* 11 (2019) 16017–16025, doi:[10.1039/c9nr05204f](https://doi.org/10.1039/c9nr05204f).
- [36] Y. Qiu, Q. Jia, S. Yan, B. Liu, J. Liu, X. Ji, Favorable amorphous–crystalline iron oxyhydroxide phase boundaries for boosted alkaline water oxidation, *ChemSusChem* 13 (2020) 4911–4915, doi:[10.1002/cssc.202001229](https://doi.org/10.1002/cssc.202001229).
- [37] J. Dong, Y. Wang, Q. Jiang, Z.A. Nan, F.R. Fan, Z.Q. Tian, Charged droplet-driven fast formation of nickel–iron (oxy)hydroxides with rich oxygen defects for boosting overall water splitting, *J. Mater. Chem. A* (2021), doi:[10.1039/d1ta05332a](https://doi.org/10.1039/d1ta05332a).
- [38] C. Hobbs, S. Jaskaniec, E.K. McCarthy, C. Downing, K. Opelt, K. Güth, A. Shmeliov, M.C.D. Mourad, K. Mandel, V. Nicolosi, Structural transformation of layered double hydroxides: an *in situ* TEM analysis, *Npj 2D Mater. Appl.* 2 (2018), doi:[10.1038/s41699-018-0048-4](https://doi.org/10.1038/s41699-018-0048-4).
- [39] Y. Tong, H. Mao, P. Chen, Q. Sun, F. Yan, F. Xi, Confinement of fluorine anions in nickel-based catalysts for greatly enhancing oxygen evolution activity, *Chem. Commun.* 56 (2020) 4196–4199, doi:[10.1039/d0cc01215g](https://doi.org/10.1039/d0cc01215g).
- [40] S. Lee, L. Bai, X. Hu, Deciphering iron-dependent activity in oxygen evolution catalyzed by nickel–iron layered double hydroxide, *Angew. Chem. Int. Ed.* 59 (2020) 8072–8077, doi:[10.1002/anie.201915803](https://doi.org/10.1002/anie.201915803).